ADVANCING SUPER RESOLUTION MICROSCOPY FOR QUANTITATIVE IN-VIVO IMAGING OF CHROMATIN NANODOMAINS

PHD PRELIMINARY EXAMINATION

DEPARTMENT OF PHYSICS

BY

CLAYTON W. SEITZ

FALL 2023

TABLE OF CONTENTS

ABSTRACT

Single-molecule localization microscopy (SMLM) techniques, such as direct stochastic optical reconstruction microscopy (dSTORM), can be used to produce a pointillist representation of fluorescently-labeled biological structures at diffraction-unlimited precision. Direct STORM approaches leverage the deactivation of standard fluorescent tags, followed by spontaneous or photoinduced reactivation, allowing resolution of fluorophores at distances below the diffraction limit. This basic principle remains one of the method's primary limitations - standard SMLM fitting routines require tight control of activation and reactivation to maintain sparse emitters, presenting a tradeoff between imaging speed and labeling density. Here, I present two parallel projects, which aim to push the current state of the art in SMLM and apply SMLM to the study of gene regulation. The former represents a novel localization technique for dense SMLM, based on deep probabilistic modeling and photon statistics. In the latter, conventional dSTORM is adapted for live cell imaging of chromatin nanodomains, demonstrating that BRD4 protein concentrates in nucleosome depleted regions.

1 Introduction

1.1 Single molecule localization microscopy

Single molecule localization microscopy (SMLM) relies on the temporal resolution of fluorophores in the sample whose spatially overlapping point spread functions would otherwise render them unresolvable at the detector. SMLM techniques, such as stochastic optical reconstruction microsscopy (STORM) and photo-activated localization microscopy (PALM) remain desirable for super-resolution imaging of many cellular structures, due to their cost-effective implementation and diffraction unlimited resolution (Schermelleh 2019). Common strategies for the temporal separation of molecules involve transient intramolecular rearrangements to switch from dark to fluorescent states or the exploitation of non-emitting molecular radicals. For direct STORM, rhodamine derivatives can undergo intersystem crossing to a triplet state, which can be reduced by thiols to form a dark radical species. The dark state can then be quenched by oxidative processes, driving the fluorophore back to its ground state (Figure 1a). Long dark state lifetimes are commonly used in STORM imaging in order to maintain sparse activation and high resolution.

1.2 The definition of resolution in SMLM

The distribution of a particular biomolecule in the cell can be described as a probability density over a two-dimensional space, casting super-resolution as a density estimation problem. Intuitively, the spatial resolution of SMLM images then increases as we draw more samples from this density - a concept which is made mathematically precise by the so-called Fourier ring correlation or FRC. Using FRC, one can compute image resolution as the spatial frequency at which a correlation function in the frequency domain drops below a threshold, typically taken to be 1/7 (Figure 2). According to this theory, reducing localization uncertainty while increasing the number of samples, results in an increase in image resolution

(Nieuwenhuizen 2013). However, there of course remains a fundamental limit to the the minimal localization uncertainty which can be obtained.

Localization uncertainty, typically the RMSE of a maximum likelihood or similar statistical estimator, is bounded from below by the inverse of the Fisher information matrix, known as the Cramer-Rao lower bound (Chao 2016). Localization uncertainties in sparse conditions are often tens of nanometers, although recent work on integration of Bayesian priors with modulation enhanced SMLM (meSMLM) or structured illumination with MINFLUX, has reduced spatial resolution below to a few nanometers (Kalisvaart 2022, Gwosh 2020). Nevertheless, managing the increase in localization uncertainty at high labeling density remains a major bottleneck to SMLM. Static uncertainty due to molecular crowding can be partially amelioriated by using pairwise or higher-order temporal correlations within a pixel neighborhood, known as stochastic optical fluctuation imaging or SOFI (Dertinger 2009). Other approaches such as stimulated emission and depletion (STED) imaging bring control over the photophysical state of a chosen subset of the sample, yet the need for laser scanning prevents widespread application in live-cell studies. The spatial resolution and relative simplicity of SMLM techniques remains unmatched, inciting an effort to increase the resolution of SMLM techniques and explore avenues towards time resolved SMLM.

1.3 Towards time-resolved SMLM

Previous approaches to improving the resolution of SMLM by increasing number of localizations per unit time have been primarily based on a combination of intensity measurements and probabilistic deep learning. Standard postprocessing for STORM imaging includes maximum likelihood estimation of molecular coordinates using Gaussian point spread function models. However, in dense STORM, the parameter space volume grows exponentially with the number of emitters, which is often unknown apriori. Exploration of this high dimensional parameter space in dense STORM is often intractable.

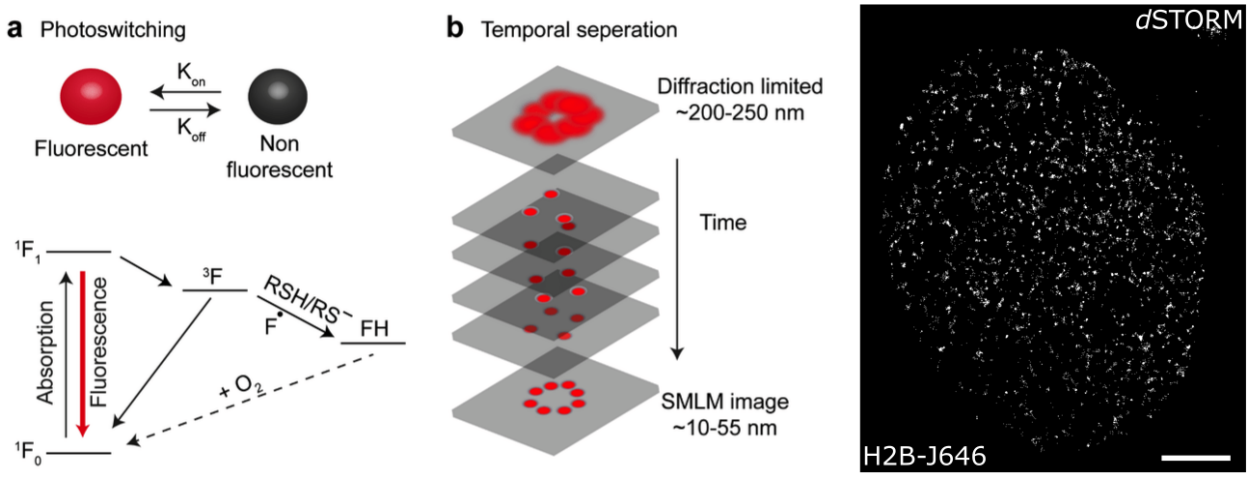

Figure 1: Stochastic optical reconstruction microscopy (STORM). (A) Single molecules are resolved by separating their fluorescent emission in time, using fluorophores with multiple photophysical states (B) Example super-resolution image of H2B protein in a living Hela cell nucleus at 37C, 5 percent CO2. Scalebar 5um.

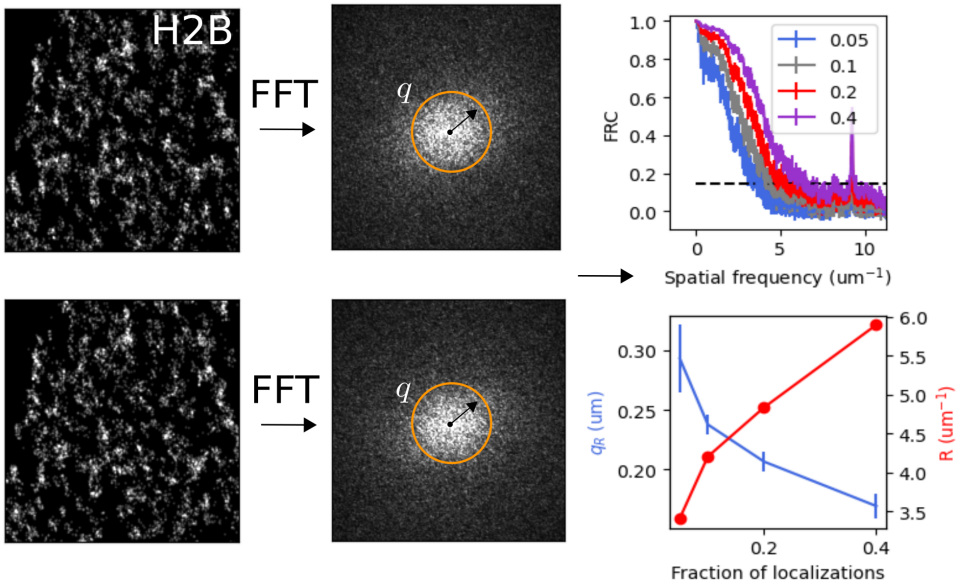

Figure 2: Dense localization increases image resolution and enables time-resolved STORM. A pair of subsets is drawn from the full list of localizations for various fractions of the total number, and isotropic Gaussian kernel density estimation is performed with $\sigma = 20$nm. The Fourier Ring Correlation (Methods) is calculated for the pair and plotted as a function of spatial frequency. R is the spatial frequency where FRC crossed the threshold (dashed line). $q_R = 1/R$, errors on q_R drawn at one standard deviation ($n = 5$).

In one approach to this issue, deep generative models have been used to learn the generating distribution of images of cellular structures from super-resolution data. Trained models can then be used to predict super-resolution images based on sparse localizations or widefield images (Ouyang 2018; Barth 2020; Chen 2023). Other approaches leverage convolutional neural networks (CNNs) to transform dense images into a localization map (Nehme 2020; Speiser 2021). In general, convolutional neural networks are well-known for their ability to discover higher order spatial structure in an image to infer latent variables. This can be seen as learning a translation from SMLM image intensities to pixel-wise probabilities of emitter occupancy.

While the use of deep models has shown great promise for dense SMLM, there remains two major drawbacks. First, CNNs are often unconstrained by physical variables, such as the total number of fluorescent emitters in a given region of interest. Second, CNNs do not explicitly model the image likelihood, making computation of localization uncertainties challenging. Therefore, we introduce a novel inference scheme which (i) infers the number fluorescent emitters in the ROI by modeling photon statistics measured with a photon counting camera (ii) permits relatively fast computation of localization uncertainty using a gradient-based Markov Chain Monte Carlo (MCMC) scheme, known as Langevin dynamics.

1.4 Enhanced SMLM with photon statistics

Molecular counting with photon statistics has a fairly simple motivation: a photon emitted by a fluorescent molecule can only be detected once. Coincidence of photons at multiple detector elements provides evidence that two or more molecules are present in the imaged region. Combining the ideas of conventional super-resolution approaches, such as dSTORM, with photon statistics may prove to be a powerful set of methods for bioimaging. Innovations in single photon detection technologies have begun to be integrated into fluorescence microscopes (Forbes 2019). Importantly, single photon detectors such as single

photon avalanche photodiodes (SPAD) arrays have three orders of magnitude higher temporal resolutions than standard sCMOS cameras, single photon sensitivity, and theoretically zero readout noise. Such properties make these devices highly desirable for imaging applications; however, application of SPAD arrays in imaging have been limited to small bundles of detector elements combined with laser scanning (Israel 2017; Forbes 2019; Tenne 2019). Recently, SPAD cameras have become commercially available, potentially bringing many of the advantages of single photon detection to widefield fluorescence microscopy. As a proof of principle, we image quantum dots (QDs) at 1 MHz with a 512x512 SPAD array, and introduce a fully probabilistic model for dense localization microscopy (See Future Aims). Our results demonstrate that, after pixel-size correction, the SPAD sensor maintains 50 percent quantum efficiency of CMOS (Figure 4). However, using increased magnification retains the ability to localize single QDs.

1.5 Super-resolution of chromatin nanodomains in living cells

Super-resolution imaging with intensity information alone remains a highly valuable technique, and we demonstrate this by live cell super-resolution of nucleosome-BRD4 interactions in Hela cell nuclei. The nucleosome is the fundamental unit of chromatin - a complex of DNA and protein which forms the basic scaffold for a variety of biomolecular processes in the nucleus. Super-resolved nucleosome organization has been studied extensively in various epigenomic states to reveal segregated nanoclusters, dispersed nanodomains, and compact large aggregates. Indeed, nucleosomes assemble into heterogeneous clusters of variable sizes, interspersed with nucleosome-depleted regions (Ricci 2015). Histones can be decorated with various post-translational modifications such as acetylation, methylation, phosphorylation, and ubiquination. The recruitment of proteins and complexes with specific enzymatic activities is now a well-accepted dogma of how modifications mediate their function. Histone modifications can influence the transcription of genes, and many other DNA processes such

as repair, replication and recombination (Bannister and Kouzarides, 2011).

Here, we use a direct STORM approach to study spatial organization of nucleosomes in living cells, with a particular focus on the structure of phase separated condensates containing bromodomain protein 4 (BRD4) protein. BRD4 plays an important role in diverse cellular functions such as transcription, replication, epigenetic regulation, and DNA repair, and has been implicated in cancer and autoimmune diseases. BRD4 acetylates Lysine 122 on H3 (H3K122), a residue critical for nucleosome stability, resulting in nucleosome eviction and chromatin decompaction (Devaiah 2016). The intrinsically disordered regions (IDRs) of BRD4 are thought to facilitate its phase separation with coactivators such as MED1. The phase separation properties of BRD4 have been well-studied in several cell lines (Han 2020), and in the context of super-enhancers (Sabari 2018).

Selective bromodomain inhibitors, such as JQ1 are often used to impair the chromatin-reading function, displacing BRD4 protein from chromatin (Filippakopoulos 2010). Also, 1,6-hexanediol (1,6-HD), an aliphatic alcohol, can inhibit weak hydrophobic protein-protein interactions required for droplet formation and is widely used to elucidate the formation of nuclear bodies (Duster 2021). However, the relationship of BRD4, and phase separation at large, with the spatial structure of nucleosome nanodomains remains unclear. As BRD4 is a critical component of phase separated transcriptional condensates, we take a complementary approach, consisting of specific and non-specific inhibition of BRD4-containing condensates using small molecule drugs and BRD4 mutation or knockdown. Our preliminary results indicate the BRD4 is primarily present in nucleosome depleted regions and the chromatin reading function in necessary for the maintenance for chromatin structure.

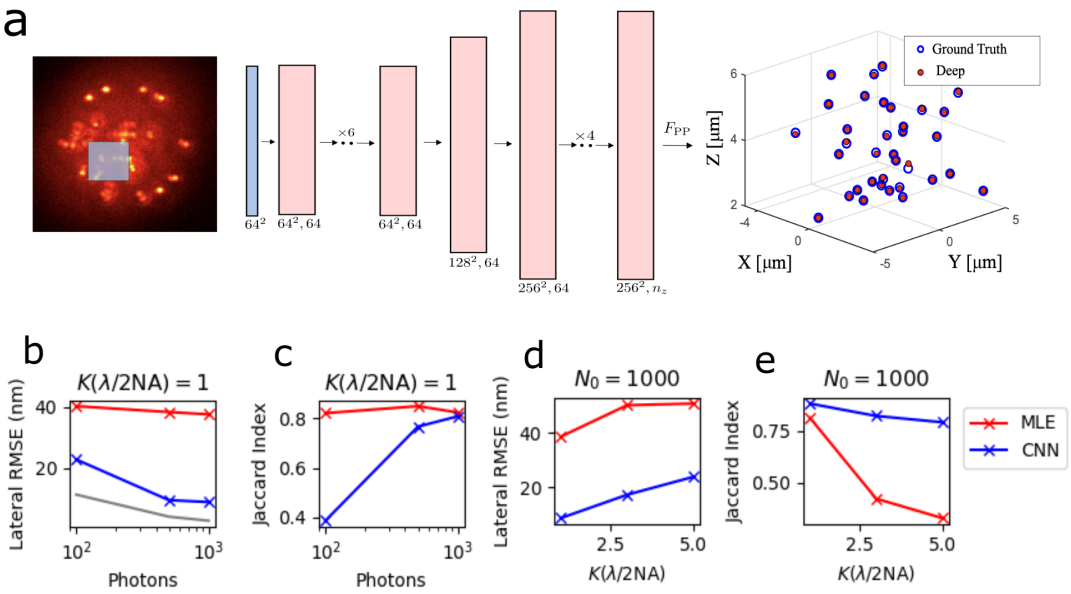

Figure 3: Deep networks outperform MLE in dense localization (A) DeepSTORM architecture with 612K trainable parameters used for localization. (B-E) Lateral root mean squared error and Jaccard index of MLE and CNN estimators with respect to the incident photon count and the number of molecules within the diffraction limit. 10^3 images simulated by drawing K coordinate pairs uniformly on a disc of radius $\lambda/2\text{NA}$, assuming $\lambda = 640\text{nm}$. Cramer-Rao lower bound shown in gray

2 Results

2.1 Deep networks outperform MLE in dense localization

Two major factors contribute to localization errors in SMLM: (i) the noise characteristics of CMOS cameras and (ii) crowding of molecules within a diffraction limited region. Maxmimum likelihood estimation (MLE) is frequently used for isolated molecules and high signal levels, retaining localization errors 40nm (Figure 3b). However, MLE performance tends to degrade in low SNR and dense regimes where the number of emitters within the diffraction limit is greater than one ($K(\lambda/2\text{NA}) > 1$). We employ a convolutional neural network called DeepSTORM, which successively upsamples a monochrome image and outputs a localization map, which can be post-processed to produce molecular coordinates in 2D or 3D (Figure 3a). We demonstrate that this architecture can outperform maximum likelihood estimation

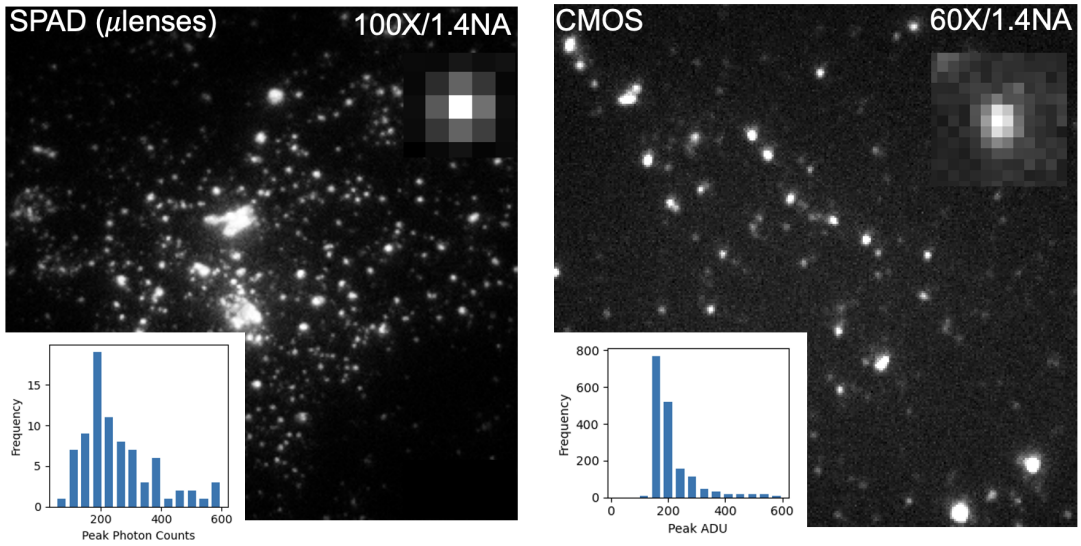

Figure 4: SPAD cameras sacrifice sensitivity for speed. (left) Quantum dots imaged with a SPAD camera using 100X/1.4NA oil immersion objective with continous-wave 640nm laser excitation. Image is a sum of 10^4 1us exposures. (left inset) Peak photon counts of isolated QDs using SPAD. (right) Quantum dots imaged with 10ms exposure of a CMOS camera using 60X/1.4NA oil immersion objective with continous-wave 640nm laser excitation. (right inset) Peak photon counts of isolated QDs using CMOS (right). SPAD pixel size is 160nm and CMOS is 108nm.

for all signal levels and molecular densities tested (Figure 3b-e).

2.2 Imaging quantum dots with a photon counting camera

Dense aggregates of proteins and nucleic acids with molecular spacing below the diffraction limit are commonplace in the nucleus, creating the need for accurate counting techniques. The ability to accurately count fluorescent emitters using photon statistics has been so far limited to confocal microscopy setups, which are not typically used when imaging dynamics in living cells. As a proof of principle, we imaged quantum dots (QDs): 15-20nm nanocrystals composed of a CdSe semiconductor core and ZnS semiconductor shell, coated on a glass coverslip. QDs were imaged with a SPAD camera at 1 MHz, to compare the sensitivity ratio of SPAD and CMOS, while measuring photon statistics from isolated QDs and aggregates

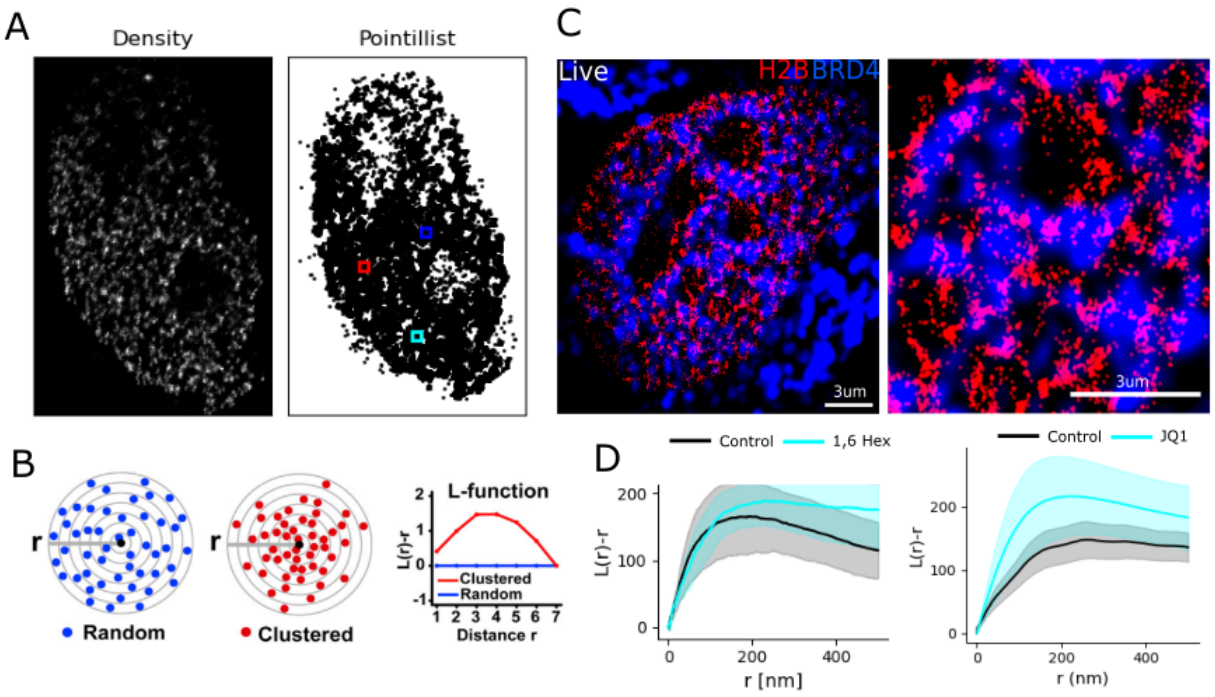

Figure 5: Super-resolution of nucleosome-BRD4 interactions in living cells. (A) Density and pointillist representation of nucleosome organization in a living cell recovered with MLE-CMOS (B) Principle of Besag's L-Function for cluster analysis (C) Two color image with super-resolved nucleosomes and diffraction limited BRD4 signal. (D) Average L-function for living Hela cells exposed to 5 percent 1,6 Hexanediol or 1uM JQ1 for 8h. Envelope drawn at one standard deviation

(Figure 4). We found that, after pixel size correction due to relatively large SPAD pixels, the sensitivity of SPAD is reduced by a factor of two. However, the device still brings many of the benefits of high speed imaging.

2.3 Super-resolution of nucleosome-BRD4 interactions in living cells

Here, we use the HaloTag system, a modified haloalkane dehalogenase designed to covalently bind to synthetic ligands (Los 2008). The HaloTag protein is fused to H2B and is then bound by a rhodomine-derived fluorescent ligands, JF549 or JF646 (Grimm 2015). Two-color imaging of H2B-JF646 and BRD4-GFP showed that BRD4-GFP is present in nucleosome

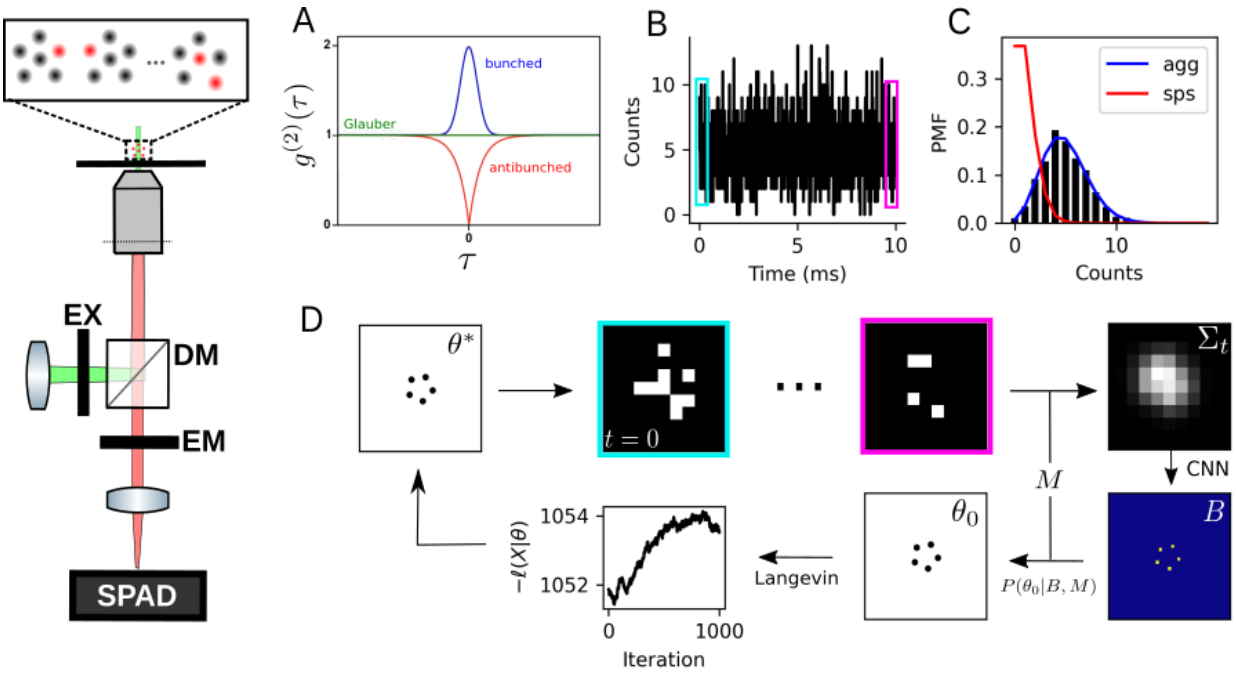

Figure 6: Blending deep models and single photon counting for enhanced SMLM. (left) Simplified schematic of microscopy setup (A) Conceptual figure of the coherent state with Poisson statistics: $g^{(2)}(\tau) = 1$ (B) Photon counts in 1us from an aggregate of QDs over 10ms. (C) Distribution of photon counts in 1us for an isolated QD (sps) and an aggregate (agg). (D) Schematic of inference process - see Future Aims for details

depleted regions, and that BRD4-GFP makes direct contact with the chromatin scaffold (Figure 5c). Exposure of cells to 1,6 Hexanediol promoted an increase in nucleosome cluster sizes, while JQ1 exposure significantly condensed nucleosome clusters (Figure 5d).

3 Discussion and Future Aims

3.1 Specific Aim 1: Integrate deep models with counting algorithms for enhanced SMLM

Rationale and hypothesis

We have demonstrated that deep learning algorithms can outperform standard maximum likelihood estimators in low SNR and high density regimes, indicating this is a suitable first step in our SMLM pipeline. In addition, modeling photon statistics using high speed imaging has shown promise as a pathway to rigorously counting fluorescent molecules in the sample. To be clear, at high speeds we can divide a $\Delta = 10$ms exposure into $\Delta = 1 - 10$us frames. Thus we obtain both spatial information needed for localization as well as thousands of samples from the distribution on photon counts. In other words, using long exposures like $\Delta = 10$ms is wasteful, and it would take potentially seconds to obtain a similar number of samples for estimating a value for M.

Computational Approach

We maximize the posterior probability $P(\theta|X)$, where θ are molecular coordinates and X is a time series of photon counts.

$$\begin{aligned}\theta_{\text{MAP}} &= \underset{\theta,\Psi}{\text{argmax}}\ P(\theta|X) \\ &= \underset{\theta,\Psi}{\text{argmax}}\ P(\theta|\theta_0)P(\theta_0|B,M)P_\Psi(B|S)P(M|X)\end{aligned}$$

The distribution on photon counts $P(X|M) = P(M|X)$ is Poisson, assuming the bright state of the fluorophore is highly stable, giving a coherent state (Vlasenko 2020). Let $\mu_0 =$

$\lambda_0\Delta$ be the measured rate parameter for an isolated fluorophore. By imaging at high speeds of 1MHz i.e., $\Delta = 1$us, we obtain samples from $P(X|M)$ and can fit X with a model Poisson($\mu_0 m$) for some integer m and perform model selection on m.

A convolutional neural network Ψ predicts B from S (the time sum of X). B represents a Bernoulli probability at each pixel. We then select the initial condition θ_0 by rejection sampling of M objects conditioned on B. Finally, we can measure the quality of θ_0 by using gradient-based MCMC to explore the parameter space surrounding θ_0. Specifically, we modifying the likelihood in (5) to account for multiple emitters and zero readout noise

$$\mu'_k = \mu_k = \sum_{m=1}^{M} \mu_{k,m}$$

Then, by computing gradients of (5) as before, we have the Langevin update rule (Welling and Teh 2011)

$$\theta_{t+1} = \theta_t + \frac{\epsilon}{2}\nabla\ell(\theta_t) + \sqrt{\epsilon}\cdot\mathcal{N}(0, I)$$

where ϵ is called the step-size. By obtaining samples of θ we can compute important statistics such as $\langle\ell\rangle$ as a quality metric for θ_0.

3.2 Specific Aim 2: Determine a role of chromatin architecture in BRD4 phase separation

Rationale and hypothesis

Condensation of nucleosome clusters as well as cluster growth following exposure to JQ1 suggests that BRD4 may play a multiple important roles in the maintenance of chromatin architecture. BRD4-GFP is clearly present in nucleosome depleted regions; however, there remains a significant overlap of H2B and BRD4 signals. Interestingly, the BRD4-GFP signal

also appears continuous at the border of nucleosome clusters. This leads us to believe that BRD4 condensates permeate both nucleosome-dense and sparse regions. We hypothesize that BRD4 can phase separate with both chromatin as well as other cofactors in NDRs to simultaneously maintain condensed chromatin clusters and nucleosome-depletion. Corroborating this duality, previous approaches in epigenomics, proteomics and chemical biology have shown that hyperphosphorylated BRD4 binds more strongly to MED1, facilitating a bromodomain-independent chromatin recruitment mechanism (Shu 2016).

Experimental Approach

We propose super-resolution experiments to determine if indeed BRD4 possesses this duality. To do this, we have designed siRNAs to knockdown expression of BRD4 protein in Hela cells, which will determine the effect of global BRD4 loss on chromatin architecture. We will first validate our previous experiments with JQ1 by expressing a FLAG-tagged BRD4 mutant with mutated Bromodomains (BDmut) to determine the impact on nucleosome clustering. Next, we will transfect constitutively phosphorylated BRD4 plasmids and expose cells to JQ1. The organization of BRD4 in the nucleus can then be readily compared to global phase separation inhibitors like 1,6 Hexanediol. Finally, in order to address the possibility that small molecule drugs such as JQ1 impact structure of the chromatin scaffold, independent of BRD4, we will carry out additional live-cell super-resolution experiments combining BRD4 RNA silencing with JQ1 exposure.

4 Materials and Methods

4.1 Super-resolution imaging of nucleosome nanodomains

After transient transfection, H2B-Halotag Hela cells were incubated with JF646 HaloTag ligand overnight. Living Hela cells were imaged in a dSTORM photoswitching buffer containing

100mM MEA, 50 ug/ml Glucose Oxidase, and 3.4 mg/ml Catalase (Sigma). Buffer pH was adjusted to 8 using HCl. Movies were collected using a customized Olympus IX83 microscope equipped with an Olympus 60X 1.25NA oil-immersion objective. Fluorescence images were projected onto an ORCA-Fusion sCMOS camera (Hamamatsu). The microscope was controlled using Micromanager software. JF646 molecules were illuminated with a 640nm laser held at 20mW, as measured at the back focal plane of the objective. Frames were captured at 100fps. Sparse localizations were localized with maximum likelihood estimation.

4.2 Localization with maximum likelihood estimation (MLE-CMOS)

For each pixel of a CMOS camera, the number of photoelectrons S_k is multiplied by a gain factor g_k [ADU/e^-], which we have previously measured to have a tight distribution around unity. The readout noise per pixel ξ_k is Gaussian with some pixel-specific offset o_k (Figure 7a) and variance σ_k^2 (Figure 7b). Ultimately, we have a Poisson component of the noise, which scales with the signal level and a Gaussian component, which does not. Therefore, in a single exposure, we measure:

$$\vec{H} = \vec{S} + \vec{\xi} \tag{1}$$

What we are after is the joint distribution $P(\vec{H})$. Fundamental probability theory states that the distribution of H_k is the convolution of the distributions of S_k and ξ_k,

$$P(H_k|\theta) = P(S_k) \circledast P(\xi_k) \tag{2}$$

$$= A \sum_{q=0}^{\infty} \frac{1}{q!} e^{-\mu_k} \mu_k^q \frac{1}{\sqrt{2\pi}\sigma_k} e^{-\frac{(H_k - g_k q - o_k)}{2\sigma_k^2}} \tag{3}$$

where $P(\xi_k) = \mathcal{N}(o_k, \sigma_k^2)$ and $P(S_k) = \text{Poisson}(g_k \mu_k)$, A is some normalization constant

and $\circledast$ represents convolution. The rate μ_k is computed by the forward model which is an integration of the point spread function of the microscope (Supp. Eq 8). In practice, (3) is difficult to work with, so we look for an approximation. We will use the Poisson-Normal approximation for simplification. Consider,

$$\xi_k - o_k + \sigma_k^2 \sim \mathcal{N}(\sigma_k^2, \sigma_k^2) \approx \text{Poisson}(\sigma_k^2)$$

Since $H_k = S_k + \xi_k$, we transform $H'_k = H_k - o_k + \sigma_k^2$, which is distributed according to

$$H'_k \sim \text{Poisson}(\mu'_k)$$

where $\mu'_k = g_k \mu_k + \sigma_k^2$. This result can be seen from the fact the the convolution of two Poisson distributions is also Poisson. The quality of this approximation will degrade with decreasing signal level, since the Poisson distribution does not retain its Gaussian shape at low expected counts. Nevertheless, the quality of the approximation appears to increase exponentially with the expected count, as measured by the Komogonov distance between the convolution distribution (4) and its Poisson approximation (Figure 8).

In this work, we suppose that molecules really do have an exact location in space over the integration interval. In pratice, this is only an approximation since molecules can diffuse at physiological temperatures, and our exposure time would need to tend to zero for this to be exactly true. If we suppose that we can collect a sufficient amount of photons in a short enough time, such that a definite position exists, the following optimization problem is defined

$$\theta_{\text{MLE}} = \underset{\theta}{\text{argmax}} \prod_k P(H_k|\theta) = \underset{\theta}{\text{argmin}} - \sum_k \log P(H_k|\theta)$$

where θ_{MLE} represents the maximum likelihood coordinates of a fluorescent molecule. Maximum likelihood estimation (MLE) is a natural choice, since optimization of coordinates

under a Poisson likelihood is tractable. Under the Poisson approximation, the model negative log-likelihood is

$$\ell(\vec{H}|\theta) = -\log \prod_k \frac{e^{-(\mu'_k)} \left(\mu'_k\right)^{n_k}}{n_k!} \tag{4}$$

$$= \sum_k \log n_k! + \mu'_k - n_k \log\left(\mu'_k\right) \tag{5}$$

A stirling approximation can be made for the above log-factorial. First order derivatives of this sum can often be computed analytically, depending on μ.

To summarize, out localization method depends on a likelihood for independent Poisson variables, where the parameter of each Poisson variable is a function of other latent variables (molecular coordinates). The full distribution over images $\vec{H}$ cannot be written down explicitly - it can only be written at a single point in parameter space. We compute the rates μ first using the forward model (Supp. Eq 8) and then compute the Poisson data likelihood using calculated rates. This intermediate step is what prevents us from being able to write down a likelihood only in terms of common distributions.

4.3 The Cramer-Rao lower bound

The Poisson approximation is also convenient for computing the Fisher information matrix for θ_{MLE} and thus the Cramer-Rao lower bound, which bounds the variance of a statistical estimator of θ_{MLE}, from below (Chao 2016). THe Fisher information is

$$I_{ij}(\theta) = \mathop{\mathbb{E}}_{\theta}\left(\frac{\partial \ell}{\partial \theta_i}\frac{\partial \ell}{\partial \theta_j}\right) \tag{6}$$

Let $\mu'_k = \mu_k + \sigma_k^2$. For an arbitrary parameter,

$$\frac{\partial \ell}{\partial \theta_i} = \frac{\partial}{\partial \theta_i} \sum_k x_k \log x_k + \mu'_k - x_k \log\left(\mu'_k\right)$$
$$= \sum_k \frac{\partial \mu'_k}{\partial \theta_i} \left(\frac{\mu'_k - x_k}{\mu'_k} \right)$$

$$I_{ij}(\theta) = \mathop{\mathbb{E}}_{\theta} \left(\sum_k \frac{\partial \mu'_k}{\partial \theta_i} \frac{\partial \mu'_k}{\partial \theta_j} \left(\frac{\mu'_k - x_k}{\mu'_k} \right)^2 \right) = \sum_k \frac{1}{\mu'_k} \frac{\partial \mu'_k}{\partial \theta_i} \frac{\partial \mu'_k}{\partial \theta_j}$$

4.4 Dense localization with convolutional neural networks

We employ a localization CNN architecture based on DeepSTORM which consists of three main modules. A complete mathematical description of the architecture is given in the original paper (Nehme 2020). The first module consists of successive dilated convolutions, followed by an upsampling module to increase the lateral resolution by a factor of 4. The third and last module adds additional convolutional blocks to refine localization estimates. This architecture can also be used for three-dimensional localization and thus the final output has n_z channels. The final output is followed by an element-wise HardTanh (Maas 2013). A post-processing function F_{PP} uses a user-defined threshold to produce a matrix of coordinates. We find the performance of this architecture on simulated images surpasses MLE, and approaches the Cramer-Rao lower bound at high signal levels, retaining a RMSE near 20nm for $K(\lambda/2\text{NA}) \leq 5$, at high signal levels (Figure 3).

4.5 Computation of Besag's L-function

Besag's L-function $L(r)$ is a transformation of Ripley's K-function $K(r)$. The estimates of $K(r)$ are of the form

$$K(r) = \frac{a}{n(n-1)} \sum_{ij} I(d_{ij} \leq r)$$

where a is the area of the window, n is the number of data points and the sum is taken over all pairs of points. $I(d_{ij} \leq r)$ is the indicator function which equals 1 is the distance is less than or equal to r. The L-function is then $L(r) = \sqrt{\frac{K(r)}{\pi}}$. For a stationary Poisson process $L(r) = r$, making a $L(r) - r$ a suitable choice for the degree of clustering.

4.6 Fourier Ring Correlation

Following (Nieuwenhuizen 2013), a pair of subsets is drawn from the full list of localizations, and isotropic Gaussian kernel density estimation is performed. The Fourier Ring Correlation is calculated as a function of the ring radius q for two images f_1 and f_2

$$\mathrm{FRC}(q) = \frac{\sum_{\vec{q} \in \mathrm{circle}} \tilde{f}_1(\vec{q}) \tilde{f}_2(\vec{q})^*}{\sqrt{\sum_{\vec{q} \in \mathrm{circle}} |f_1(\vec{q})|^2} \sqrt{\sum_{\vec{q} \in \mathrm{circle}} |f_2}(\vec{q})|^2}$$

where, for example, $\tilde{f}_1$ is the discrete Fourier transform of f_1.

5 Supplemental Information

5.1 Noise model for MLE-CMOS

CMOS cameras have noise sources intrinsic to their operation, such as shot noise and read-out noise. The former phenomenon can describe a superposition of processes; namely, the fluctuations of the number of photons due to the quantum nature of light, and the random conversion of photons into photoelectrons within the semiconductor material with a quantum efficiency below unity. Here we will often refer to the photon count N_0, which has a

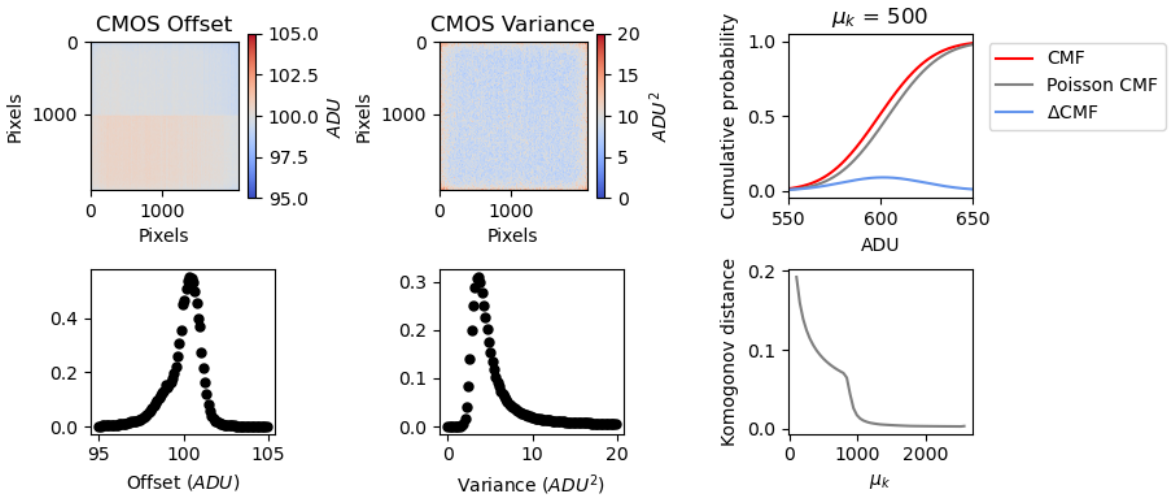

Figure 7: Noise model for CMOS cameras used for MLE. (A) Offset for zero incident photons (B) Variance for zero incident photons (C) Cumulative mass function for the convolution distribution and its Poisson approximation for rate parameter $\mu_k = 500$ counts (D) Komogonov distance measured as a function of rate parameter μ_k

determined value, rather than being described by statistically. The *measured* photon count, however, is well-described by a Poisson process (Schottky 1918). A shot-noise limited image with N pixels is then described as a family of Poisson variables, with units of photoelectrons

$$\vec{S} = [\text{Poisson}(\mu_1), \text{Poisson}(\mu_2), ..., \text{Poisson}(\mu_N)] \tag{7}$$

CMOS sensors also suffer from other noise sources, such as readout noise or dark current, resulting in a nonzero signal even in the absence of incident light. Dark current is due to statistical fluctuations in the photoelectron count within a semiconductor material in thermal equilibrium. Fortunately, these additional noise sources are governed by the central limit theorem, and can be efficiently summarized as the component of the noise which exhibits a Gaussian distribution. Readout noise has been often neglected in localization algorithms because its presence in EMCCD cameras is small enough that it can be ignored within the tolerances of the localization precision. In the case of high speed CMOS cameras, however, the readout noise of each pixel is significantly higher and, in addition, every pixel

has its own noise and gain characteristic sometimes with dramatic pixel-to-pixel variations (Huang 2013). Therefore, accurate localization and simulation necessisitates models which incorporate detailed sensor properties.

5.2 Integrated isotropic Gaussian point spread functions

For the sake of simplicity, it is common to describe the point spread function (PSF) as a two-dimensional isotropic Gaussian (Zhang 2007). This is an approximation to the more rigorous diffraction models given by Richards and Wolf (1959) or Gibson and Lanni (1989).

$$\mathrm{G}(x,y) = \frac{1}{2\pi\sigma^2} e^{-\frac{(x-x_0)^2+(y-y_0)^2}{2\sigma^2}}$$

The chracteristic width σ of the PSF typically depends on the numerical aperture of the objective lens. The image of a fluorescent molecule captured by the objective lens, can be thought of as two-dimensional histogram of photon arrivals and a discretized form of the classical intensity profile $\mathrm{G}(x,y)$. The value at a pixel approaches an integral of this density over the pixel:

$$\mu_k = i_0 \lambda_k = i_0 \int_{\text{pixel}} G(x,y)dxdy \tag{8}$$

where $i_0 = g_k \eta N_0 \Delta$. The parameter η is the quantum efficiency and Δ is the exposure time. N_0 represents the number of photons emitted per unit time. The above integral can be expressed in terms of error functions, and the full calculation can be found in (Smith 2010).

6 References

[1] Schermelleh, L. et al. Super-resolution microscopy demystified. Nature Cell Biology vol. 21 72–84 (2019).

[2] Speiser, A. et al. Deep learning enables fast and dense single-molecule localization with high accuracy. Nat Methods 18, 1082–1090 (2021).

[3] Dertinger, T., Colyer, R., Iyer, G., Weiss, S. Enderlein, J. Fast, background-free, 3D super-resolution optical fluctuation imaging (SOFI). PNAS

[4] Richards, B. Wolf, E. Electromagnetic Diffraction in Optical Systems. II. Structure of the Image Field in an Aplanatic System. Source: Proceedings of the Royal Society of London. Series A, Mathematical and Physical Sciences vol. 253 (1959).

[5] Ouyang, W., Aristov, A., Lelek, M., Hao, X. Zimmer, C. Deep learning massively accelerates super-resolution localization microscopy. Nat Biotechnol 36, 460–468 (2018).

[6] Chao, J., Sally Ward, E. Ober, R. J. Fisher information theory for parameter estimation in single molecule microscopy: tutorial. Journal of the Optical Society of America A 33, B36 (2016).

[7] Nehme, E. et al. DeepSTORM3D: dense 3D localization microscopy and PSF design by deep learning. Nat Methods 17, 734–740 (2020).

[8] Nieuwenhuizen, R et al. Measuring image resolution in optical nanoscopy. Nature Methods 10. 557-562 (2013). [9] Tokunaga, M., Imamoto, N. Sakata-Sogawa, K. Highly inclined thin illumination enables clear single-molecule imaging in cells. Nat Methods 5, (2007).

[10] Kalisvaart, D. et al. Precision in iterative modulation enhanced single-molecule localization microscopy. Biophys J 121, 2279–2289 (2022).

[11] Zhang, B., Zerubia, J. Olivo-Marin, J.-C. Gaussian approximations of fluorescence microscope point-spread function models. (2007).

[12] Smith, C. S., Joseph, N., Rieger, B. Lidke, K. A. Fast, single-molecule localization that achieves theoretically minimum uncertainty. Nat Methods 7, 373–375 (2010).

[13] Sabari, B. R. et al. Coactivator condensation at super-enhancers links phase separation and gene control. Science (1979) 361, (2018).

[14] Linde, S. Van De et al. Direct stochastic optical reconstruction microscopy with stan-

dard fluorescent probes. Nat Protoc 6, 991–1009 (2011).

[15] Huang, F. et al. Video-rate nanoscopy using sCMOS camera-specific single-molecule localization algorithms. Nat Methods 10, 653–658 (2013).

[16] Hnisz, D., Shrinivas, K., Young, R. A., Chakraborty, A. K. Sharp, P. A. A Phase Separation Model for Transcriptional Control. Cell vol. 169 13–23 (2017).

[17] Grimm, J. B. et al. A general method to improve fluorophores for live-cell and single-molecule microscopy. Nat Methods 12, 244–250 (2015).

[18] Nozaki, T. et al. Dynamic Organization of Chromatin Domains Revealed by Super-Resolution Live-Cell Imaging. Mol Cell 67, 282-293.e7 (2017).

[19] Xu, J. et al. Super-Resolution Imaging of Higher-Order Chromatin Structures at Different Epigenomic States in Single Mammalian Cells. Cell Rep 24, 873–882 (2018).

[20] Boettiger, A. N. et al. Super-resolution imaging reveals distinct chromatin folding for different epigenetic states. Nature 529, 418–422 (2016).

[21] Nozaki, T. et al. Dynamic Organization of Chromatin Domains Revealed by Super-Resolution Live-Cell Imaging. Mol Cell 67, 282-293.e7 (2017). [3] Barth, R., Bystricky, K. Shaban, H. A. Coupling chromatin structure and dynamics by live super-resolution imaging. Sci. Adv vol. 6 (2020).

[22] Devaiah, B. N. et al. BRD4 is a histone acetyltransferase that evicts nucleosomes from chromatin. Nat Struct Mol Biol 23, 540–548 (2016).

[23] Filippakopoulos, P. et al. Selective inhibition of BET bromodomains. Nature 468, 1067–1073 (2010).

[24] Grimm, J. B. et al. A General Method to Improve Fluorophores Using Deuterated Auxochromes. JACS Au 1, 690–696 (2021).

[25] Itoh, Y. et al. 1,6-hexanediol rapidly immobilizes and condenses chromatin in living human cells. Life Sci Alliance 4, (2021).

[26] Han, X. et al. Roles of the BRD4 short isoform in phase separation and active gene

transcription. Nat Struct Mol Biol 27, 333–341 (2020).

[27] Los, G. V. et al. HaloTag: A novel protein labeling technology for cell imaging and protein analysis. ACS Chem Biol 3, 373–382 (2008).

[28] Bannister, A. J. Kouzarides, T. Regulation of chromatin by histone modifications. Cell Research vol. 21 381–395 (2011).

[29] Ricci, M. A., Manzo, C., García-Parajo, M. F., Lakadamyali, M. Cosma, M. P. Chromatin fibers are formed by heterogeneous groups of nucleosomes in vivo. Cell 160, 1145–1158 (2015).

[30] Welling and Teh. Bayesian learning via stochastic gradient langevin dynamics. 2011.